

# Stellar and circumstellar activity of the Be star $\omega$ CMa<sup>\*</sup>

## III. Multiline non-radial pulsation modeling

M. Maintz<sup>1</sup>, Th. Rivinius<sup>1,2</sup>, S. Štefl<sup>3</sup>, D. Baade<sup>2</sup>, B. Wolf<sup>1</sup>, and R. H. D. Townsend<sup>4</sup>

<sup>1</sup> Landessternwarte Königstuhl, 69117 Heidelberg, Germany

<sup>2</sup> European Southern Observatory, Karl-Schwarzschild-Str. 2, 85748 Garching bei München, Germany

<sup>3</sup> Astronomical Institute, Academy of Sciences, 251 65 Ondřejov, Czech Republic

<sup>4</sup> Department of Physics & Astronomy, University College London, Gower Street, London WC1E 6BT, UK

Received 12 May 2003/ Accepted 21 August 2003

**Abstract.** The line profile variability of  $\omega$  CMa is modeled for various photospheric absorption lines of different ions as non-radial pulsation. The retrograde pulsation suggested by Baade (1982) could be confirmed. Due to rapid rotation, the line profile variability appears prograde, however. The line profiles could be reproduced in great detail, including prominent structures like “spikes” and “ramps”. These features arise naturally from the pole-on orientation of the star together with high-amplitude pulsation in  $g$ -modes, i.e. with horizontal motions being dominant. The change of the line profile variability during outbursts (understood as the beginning of phases of high brightness) reported in Paper II of this series can also be understood within the framework of non-radial pulsation if veiling effects of the circumstellar disk are taken into account. It is concluded that the coherent periodic line profile variability of the absorption lines of  $\omega$  CMa can be explained by non-radial pulsation in detail.

**Key words.** stars: oscillations – stars: individual:  $\omega$  (28) CMa – stars: emission line, Be

### 1. Introduction

The pole-on Be star  $\omega$  (28) CMa (HD 56 139, HR 2749, B3IVe,  $m_V = 4.03$  mag) has increasingly gained attention in recent years. The two main reasons for this interest are the very strong, but rare outbursts, one of which started recently in 2001 (Štefl et al. 2001, 2003b, hereafter Paper I), and the well known short periodicity, analyzed by Štefl et al. (2003a, hereafter Paper II).

The periodic line profile variability ( $lpv$ ), the first to be seen in a Be star, with  $\mathcal{P} = 1.37$  day was detected by Baade (1982). Later investigations have shown many more line profile variable Be stars, of which  $\omega$  CMa exhibits the most prominent short periodic  $lpv$  known of all Be stars. Still it can be regarded as proto-typical (Rivinius et al. 2003). The periodicity was confirmed by many authors using different data sets (e.g. Harmanec 1998; Štefl et al. 1999; Balona et al. 1999). The  $lpv$  was present at least for the past 20 years, and fully coherent between 1996 and 2000. In times of outburst, however, either phase or period may shift somewhat (Paper II). No other such coherent stellar period is known for  $\omega$  CMa.

Baade (1982) suggested  $\omega$  CMa to be a non-radial pulsator, similar to  $\beta$  Cephei stars (Ledoux 1951), where the  $lpv$  would result from non-radial pulsation ( $nrp$ ) in a single  $g$ -mode with harmonic degree  $\ell = 2$  and azimuthal order  $m = +2$ .

Balona et al. (1999) did not succeed in reproducing the  $lpv$  of He I 6678 assuming  $nrp$ , while an (ad-hoc) model based on variable local linewidth (e.g. by non-uniform micro-turbulence across the stellar surface) could reproduce the He I 6678 at least in principle. But Maintz et al. (2000), exploring a larger parameter space than considered by Balona et al. (1999), were able to model the  $lpv$  of  $\omega$  CMa not only for He I 6678, but for all lines in the visible spectrum in high detail.

In light of these contradicting results,  $\omega$  CMa can be regarded as a test case that any hypothesis about the short periodic  $lpv$  of Be stars has to explain.

This work presents and discusses the detailed  $nrp$  modeling results for  $\omega$  CMa already sketched by Maintz et al. (2000), for several photospheric absorption lines of different ions, using the  $nrp$ -simulation codes BRUCE and KYLIE by Townsend (1997b). These codes were specifically developed for modeling photospheric line profiles of rapidly rotating stars and already used successfully by Rivinius et al. (2001b) for modeling the photospheric  $lpv$  of  $\mu$  Cen.

In order to isolate the periodic  $lpv$  from variability originating in the disk, only the 32 high resolution spectra obtained with FEROS (Kaufer et al. 1999) at La Silla, Chile, in

Send offprint requests to: Th. Rivinius,  
e-mail: triviniu@lsw.uni-heidelberg.de

\* Based on observations collected at the European Southern Observatory at La Silla, Chile, 55.D-0502, 56.D-0381, 58.D-0697, 62.H-0319, 64.H-0548, and 267.D-5702.

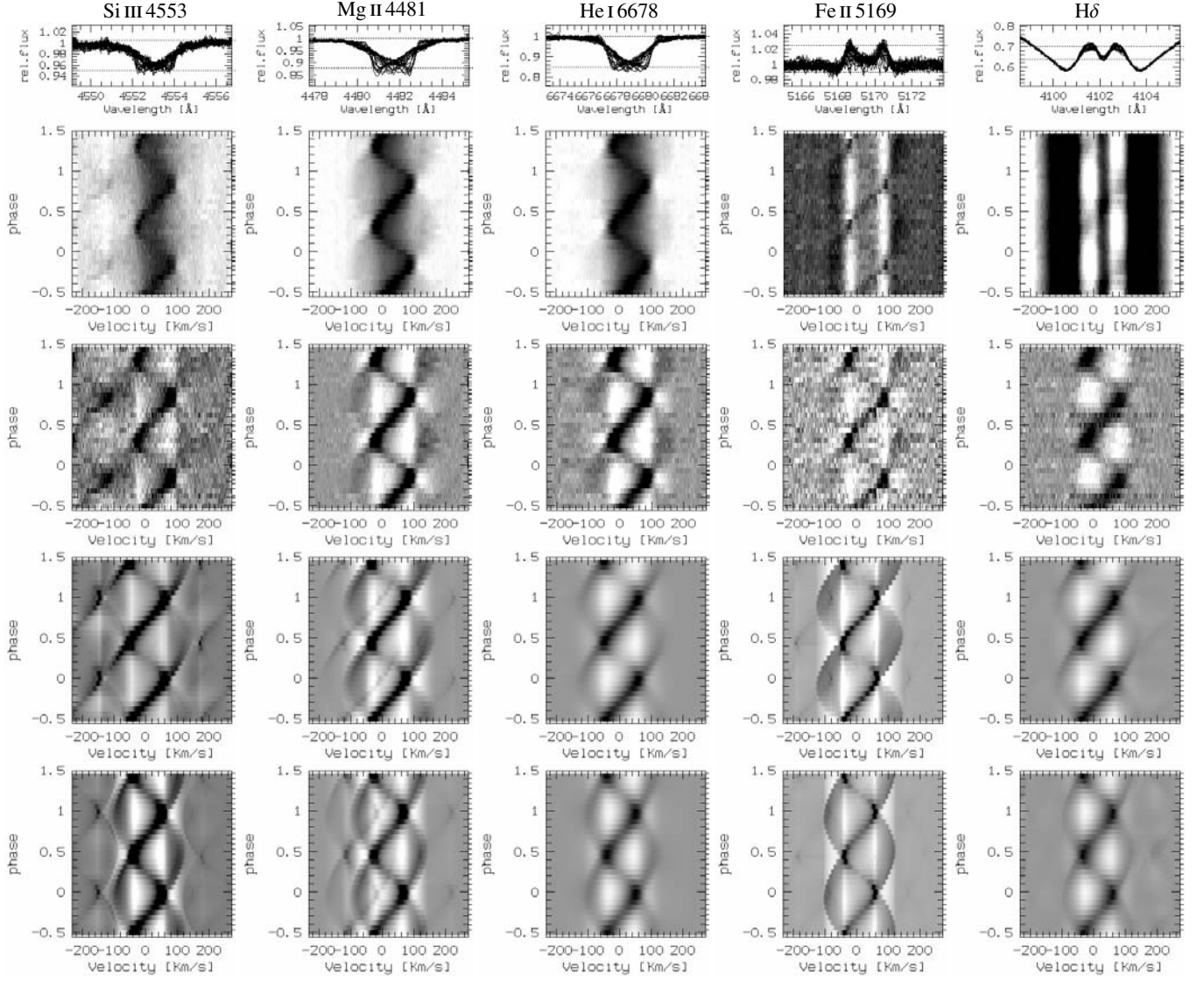


**Fig. 1.** In order to minimize the influence of the emission contribution, not the absolute line profiles (top row: overplot of spectra, second row: phased “dynamical” spectrum) are considered for modeling, but the residuals from the mean profile (third row: phased “dynamical” residuals). While the emission seems negligible in January 1999 for He I 6678 and Mg II 4481, the residuals make clear that this kind of periodic  $lpv$  is also present in Fe II 5169 or H $\delta$ , which otherwise could have been misinterpreted as variability of the emission. If in such lines the variability emerges from the disk emission or the photospheric absorption can only be clarified by comparison to emission-free lines on the one side and pure emission lines on the other one (see also Paper II). The wings of Si III 4553 are blended with Fe II lines, which, however, are also modeled. The blue side of Mg II 4481 is blended with Al III 4480 (modeled as well). The models computed with the two parameter sets giving local minima in the  $\chi^2$  distribution (see Sect. 2.3) are shown in the fourth row from top (lower  $v_{\text{rot}}$ , see Table 1) and the bottom row (higher  $v_{\text{rot}}$ , see Table 2). The velocities are given in the heliocentric system. Note the relatively high positive systemic velocity of  $\omega$  CMa. The translation of residual intensity to greyscale is kept constant for a given spectral line to enable comparison of the  $lpv$  strength between models and observations.

January 1999 (see Paper I) were taken into account for comparison with the models. Datasets taken in other seasons confirm that  $\omega$  CMa was largely in quiescence during this period, with the disk probably well detached from the stellar surface (Rivinius et al. 2001a). This choice minimizes contamination by the disk and its possible response to the  $nrp$  (e.g., transient periodicity).

The following Sect. 2 introduces the model and model parameters, while in Sect. 3 the modeling results are presented and discussed. Section 4 deals with the formation of spikes and ramps, and in Sect. 5 the change of the  $lpv$  during outbursts (as

published in Paper II) will be investigated, showing a possible solution based on  $nrp$  modeling. Final conclusions and additional perspectives arising from this series of papers on  $\omega$  CMa will be given in Sect. 6.

## 2. Non-radial pulsation modeling

As shown in Paper II, different spectral lines can exhibit different  $lpv$  properties. This is both true for one-dimensional characteristic numbers, like radial velocity amplitude, as well as for the line-profile variability viewed in two dimensions (Fig. 1).

An acceptable model must explain those differences without too many (ideally: no) additional free parameters, except the line-transition properties themselves.

The modeling technique follows closely the method described by Rivinius et al. (2001b) for the case of  $\mu$  Cen. In brief, the modeling was carried out using the *nrp*-codes BRUCE and KYLIE by Townsend (1997b), version 2.84-2. BRUCE fully includes first-order effects of rotation (Coriolis forces), but higher-order terms (like centrifugal forces) are taken into account only to compute the equilibrium configuration of the star (i.e. flattening, gravity darkening, etc.). For a further discussion of the limitations of BRUCE see Townsend (1997a,b). For a more general introduction to *nrp* modeling see also Rivinius et al. (2002b).

KYLIE then integrates the local line profiles across the visible stellar surface and so assembles the observable spectral line profile. The theoretical input line profiles required for this spectral synthesis were computed with the BHT and ATLAS 9 model codes (as described by Gummertsbach et al. 1998). For details of the used grid of synthetic input profiles see Rivinius et al. (2001b).

### 2.1. Wave propagation direction and frequency

Non-radial pulsation with  $m \neq 0$  can be imagined as a wave-pattern on the stellar surface, propagating along the equator. The number of meridional nodelines is  $2m$ , so that there are  $m$  maxima and  $m$  minima per  $2\pi$  in longitudinal direction.

Such a mode is called prograde if the wave travels in the direction of the stellar rotation (in the co-rotating stellar frame). By definition, prograde modes have negative values of  $m$  and retrograde modes have positive  $m$ . In a slow rotator, pro- and retrograde modes are well distinguishable by the observed pattern propagation (blue-to-red or red-to-blue). In a rapid rotator, however, the observed pattern might propagate from blue to red even if the *nrp* mode is retrograde in the corotating frame. This happens if the rotation frequency is higher than the pulsation frequency, meaning the rotation is more rapid than the phase velocity of the wave traveling against it.

The observed pulsational frequency and the frequency in the corotating frame are related via

$$\sigma_{\text{obs.}} = \frac{1}{\mathcal{P}_{\text{obs.}}} = \sigma_{\text{corot.}} - m\Omega \quad (1)$$

with  $\Omega$  being the rotational frequency of the star.

Defining  $\sigma_{\text{corot.}}$  and  $\Omega$  as positive values, such a high rotation and a retrograde mode can lead to a *negative* observed frequency ( $\text{sign}(\sigma_{\text{obs.}}) = -1$ ). This is nothing unphysical, but the proper mathematical expression for the situation described above. The observer is only able to determine the absolute value of the frequency, but not the sign. For the purpose of modeling, however, this doubles the parameter space to be explored.

### 2.2. Pulsational mode

During the intensive modeling of  $\mu$  Cen, it became clear that profile features like spikes and ramps could not be reproduced

for modes other than  $m = +2$  and a negative sign of the observed period. Therefore, also following Baade (1982), it was decided to concentrate on  $\ell = 2, m = +2, \text{sign}(\sigma_{\text{obs.}}) = -1$  for modeling. Numerous spot checks with other modes, including those with  $\text{sign}(\sigma_{\text{obs.}}) = +1$ , and reasonable stellar parameter sets, confirmed that the *lpv* cannot be accounted for by modes other than  $\ell = 2, m = +2$  or  $\ell = 3, m = +2$ . In a pole-on oriented star like  $\omega$  CMa, these modes do not bear strong observational differences, but the  $\ell = 3, m = +2$  mode requires higher amplitudes in temperature and geometric distortion to yield a similar reproduction of the observations as does  $\ell = 2, m = +2$ . Since the amplitudes are already quite strong, compared also to the local sound speed, for  $\ell = 2, m = +2$  this mode, with  $\text{sign}(\sigma_{\text{obs.}}) = -1$ , is adopted as the pulsational mode also of  $\omega$  CMa.

### 2.3. Model parameters

For further modeling to obtain the closest agreement between model and observations, a wide grid across plausible combinations of stellar parameters and pulsation amplitudes was computed, like for  $\mu$  Cen (Rivinius et al. 2001b, their Table 3). For  $\omega$  CMa this grid covered three polar effective temperatures (18, 20, and 22 kK), three masses (8, 9, and  $10 M_{\odot}$ ), five polar radii (4.5, 5, 5.5, 6, and  $6.5 R_{\odot}$ ), and five rotational velocities (200, 250, 300, 350, and  $400 \text{ km s}^{-1}$ ) at five projected values ( $v \sin i = 85, 90, 95, 100, \text{ and } 105 \text{ km s}^{-1}$ ). The limits were selected to cover all plausible parameter combinations for a star normally classified around B2-3 IV. However, as the example of  $\alpha$  Eri has shown recently, rapid rotation close to critical values may severely affect these numbers (Domiciano de Souza et al. 2003; Frémat et al. 2003).

Close to local minima, a finer grid mesh was used (Rivinius et al. 2001b, their Table 5). In total, synthetic spectra for several tens of thousands of parameter sets were computed.

For each parameter set, sixteen profiles for the He I 4713 line were computed in equidistant phase steps across one pulsation cycle. For comparison, the 32 spectra observed in January 1999 with FEROS were also phase-binned into 16 steps. The He I 4713 line was chosen for its low sensitivity to circumstellar influences.

The best matching parameters were, then, determined using a  $\chi^2$ -test. For this, the residuals from the respective mean line profile over the pulsational cycle are computed, in order to minimize the effect of mismatches in the modeled equivalent width. Finally, the model and observational residuals are compared to each other to find minima in the  $\chi^2$  distribution. Such minima correspond to parameter sets giving modeled *lpv* most similar to the observed one. Two local minima were found in the  $\chi^2$  distribution. One is close to the parameters published by Maintz et al. (2000), while the other, being deeper but also narrower, is at lower rotational velocities of  $v_{\text{rot}} = 250 \text{ km s}^{-1}$ .

The  $\chi^2$  values typically range from 8 to 11 for the  $\ell = 2, m = +2$ -mode, but will be significantly higher for other modes. In order to compare the quality of the parameter sets, more spectral lines in addition to He I 4713 were computed and

**Table 1.** Stellar and pulsational input parameters for modeling the *nnp* with the lower  $v_{\text{rot}}$  of  $250 \text{ km s}^{-1}$ , giving a local minimum in the  $\chi^2$  distribution discussed in Sect. 2.3. Also shown are several derived parameters.  $k$  is the ratio of horizontal-to-vertical velocity amplitude components. For an explanation of the meaning of the “apparent” parameters in a rapidly rotating star see Rivinius et al. (2001b, Sect. 6.1).

Input parameters	
Polar radius, $R_{\text{polar}}$	$5.0 R_{\odot}$
Polar temperature, $T_{\text{eff,polar}}$	18 000 K
Mass, $M$	$11 M_{\odot}$
Rotation, $v$	$250 \text{ km s}^{-1}$
Inclination, $i$	$24^{\circ}$
$\ell$	2
$m$	+2
$\mathcal{P}_{\text{obs.}} = \mathcal{P}_{\text{inert. frame}}$	-1.37 days
Full amplitude $A =  v_{\text{max}} $	$45 \text{ km s}^{-1}$
Derived parameters	
Rotational period, $\mathcal{P}_{\text{rot}}$	1.09 days
Critical period, $\mathcal{P}_{\text{crit}}$	0.52 days
Critical velocity, $v_{\text{crit}}$	$529 \text{ km s}^{-1}$
$\mathcal{P}_{\text{corot}}$	0.91 days
$k$	5.41
Polar gravity, $\log g$	4.08
Equatorial gravity, $\log g$	3.94
True luminosity, $\log(L/L_{\odot})$	3.321
Apparent luminosity, $\log(L/L_{\odot})$	3.363
Apparent $T_{\text{eff}}$	17 281 K
Apparent radius	$5.370 R_{\odot}$

visually compared with the observations. In the following both these parameter sets (Tables 1 and 2) are discussed.

### 3. Modeling results

#### 3.1. Line profile variation

The two lower rows of Fig. 1 show the residual variability for both selected parameter sets in grayscale representation. The residual variability of the displayed spectral lines is reproduced well, also for those of partly circumstellar origin like H $\delta$ . This includes the strong absorption peaks (“spikes”) and accompanying broad absorption wings (“ramps”) on respective opposite sides of the line profile, present in the phases of extreme asymmetry. Such structures are found in the majority of all spectral lines with variable prominence and were previously described by Baade (1982, for Mg II 4481 and He I 4471) and Štefl et al. (1999, for He I 6678). Since both parameter sets would be acceptable judged by the residual variability, further comparison is based on the variability of the absolute line profiles.

**Table 2.** Same as Table 2, but for the higher  $v_{\text{rot}}$  of  $350 \text{ km s}^{-1}$ .

Input parameters	
Polar radius, $R_{\text{polar}}$	$6.0 R_{\odot}$
Polar temperature, $T_{\text{eff,polar}}$	22 000 K
Mass, $M$	$9 M_{\odot}$
Rotation, $v$	$350 \text{ km s}^{-1}$
Inclination, $i$	$15^{\circ}$
$\ell$	2
$m$	+2
$\mathcal{P}_{\text{obs.}} = \mathcal{P}_{\text{inert. frame}}$	-1.37 days
Full amplitude $A =  v_{\text{max}} $	$35 \text{ km s}^{-1}$
Derived parameters	
Rotational period, $\mathcal{P}_{\text{rot}}$	1.10 days
Critical period, $\mathcal{P}_{\text{crit}}$	0.89 days
Critical velocity, $v_{\text{crit}}$	$436 \text{ km s}^{-1}$
$\mathcal{P}_{\text{corot}}$	0.92 days
$k$	2.65
Polar gravity, $\log g$	3.84
Equatorial gravity, $\log g$	3.28
True luminosity, $\log(L/L_{\odot})$	3.718
Apparent luminosity, $\log(L/L_{\odot})$	3.891
Apparent $T_{\text{eff}}$	19 658 K
Apparent radius	$7.606 R_{\odot}$

In Figs. 2 and 3, the variations of modeled and observed absolute line profiles are shown for both parameter sets. Several lines of different ions with presumably minimal emission contribution were selected.

Keeping in mind that the parameter sets were selected exclusively on this base of the He I 4713 residual *lpv*, both parameter sets reproduce well the absolute line profile variability in general, but also show some problems.

#### 3.1.1. Slowly rotating model

The local  $\chi^2$  minimum for this parameter set is about 6.9 (Fig. 4), compared to a mean value of about 9. The local minimum is narrow with respect to the stepsize of the coarse model grid. The modeled He I 4388 line shows that the  $\log g$  is too high for the slow  $v_{\text{rot}}$  parameters, since the wings are too broad. The same effect is even more visible in the Balmer line models. Clearly the mass-to-radius ratio is too high for a star classified as luminosity class IV. Comparing the Si II to the Si III line also makes clear that the model temperature is slightly too low. Also the low critical rotation rate of  $w = 0.5$  is very low compared to Be stars in general (see e.g. Chauville et al. 2001; Yudin 2001). On the other hand, the spikes are perfectly positioned and the line strengths are well reproduced for S II and Mg II.

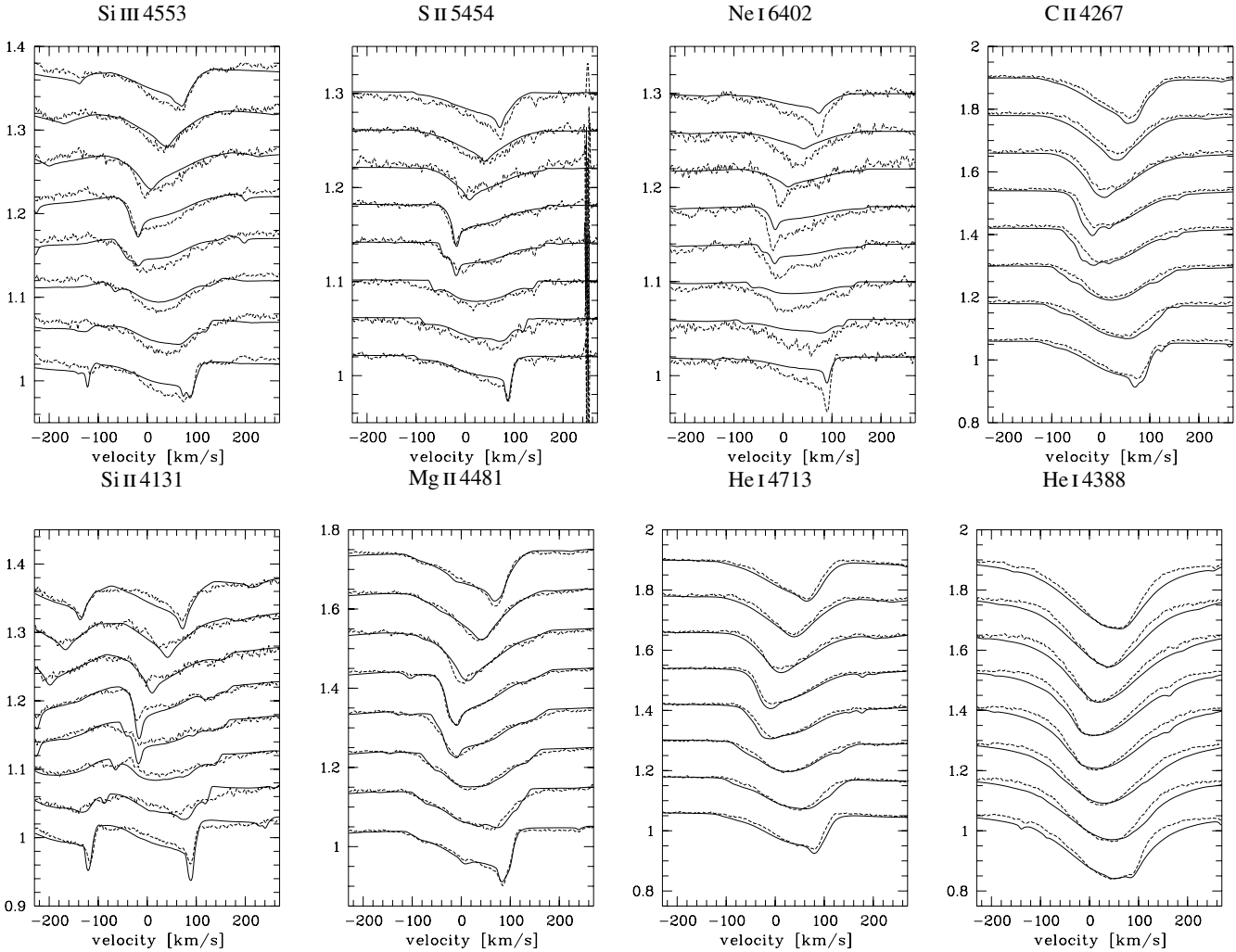


**Fig. 2.** Comparison of modeled (solid) and observed (dashed)  $lpv$  for the lower  $v_{\text{rot}}$  ( $250 \text{ km s}^{-1}$ , Table 1). Besides the spectral lines indicated on top, some panels also contain neighboring blended lines. E.g. the blue side of Mg II 4481 is blended with Al III 4480, which accounts for the small scale absorption bump at phase zero and velocity zero. Most other blends are due to Fe II lines. Phase increases from bottom to top. The observational data of S II 5454 shows CCD artifacts at about  $140 \text{ km s}^{-1}$  and  $250 \text{ km s}^{-1}$ . Only every other of the 16 computed phase steps is shown in order not to overload the plot.

### 3.1.2. Rapidly rotating model

For this minimum  $\chi^2$  reaches only 7.9 (Fig. 4), with a FWHM of about 3 times the stepsize of the coarse grid. While the lower mass and, hence, lower  $\log g$  of this parameter set reproduce the wing broadening better, the temperature is somewhat too hot and the overall reproduction of the  $lpv$  is inferior compared to the slow rotating model. Common to all modeled lines, the position of spikes, which in the model depends mostly on  $v \sin i$  and amplitude, are too close to the line center. However, the rapid rotation of  $w = 0.8$  is well in agreement with the expectation for a Be star.

### 3.1.3. Radial velocity amplitudes

The RV-amplitudes of spectral lines were found to differ both from line to line, but also from season to season (Baade 1982, Paper II). While the latter can be explained due to influences of the variable circumstellar contribution, the first is a

property of the  $lpv$  itself, and should therefore be reproduced by the model computations. Figure 5 shows the amplitudes of nine spectral lines (He I 4387, 4471, 4713, 6678, 4026, 4144, Mg II 4481, Ne I 6402, and Si III 4553) measured in the observations (Table 2 of Paper II) and for both model parameter sets. Both agree in general well. But while the rapidly rotating model is slightly worse for lines with high RV-amplitude, the slowly rotating one fails completely for two of the lines with low RV-amplitude, namely He I 4026 and 4144.

### 3.2. Stellar shape, temperature and light variations

The spatial displacements of parts of the photosphere due to pulsation are quite small. For the high- $v_{\text{rot}}$  set of parameters the radial displacements are less than 4% of the stellar radius, and the horizontal ones ( $\varphi$ - and  $\theta$ -direction) are less than 2% of the stellar circumference (Maintz et al. 2000).

Still, the temperature on the stellar surface may vary by several thousands of Kelvin locally at the equator. But, because of

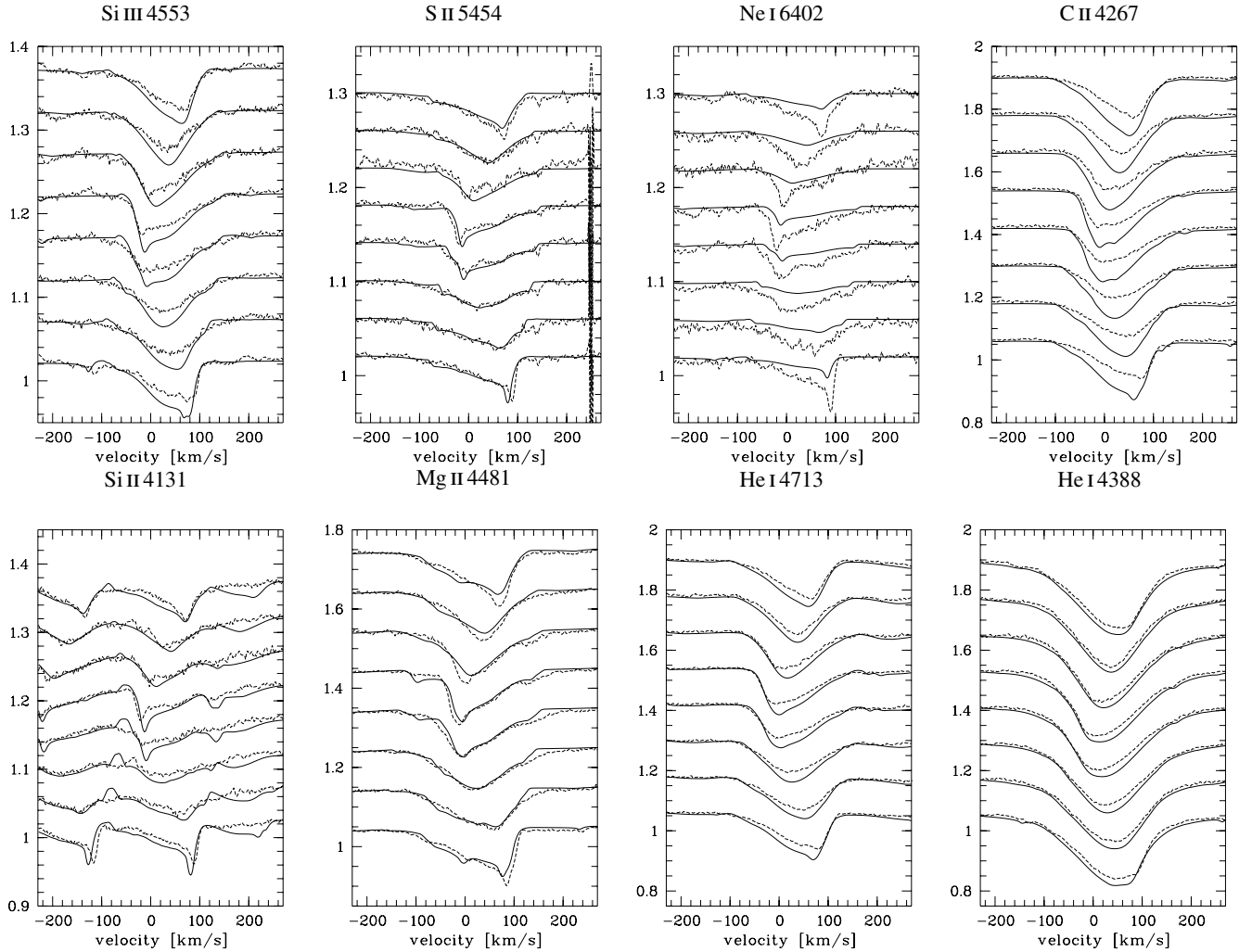


**Fig. 3.** Like Fig. 2, but for the higher  $v_{\text{rot}}$  ( $350 \text{ km s}^{-1}$ , Table 2).

cancellation effects due to the low inclination and the symmetry of the  $\ell = 2, m = 2$  mode, the disk-averaged temperature remains almost constant. Therefore, photometric measurements and the spectral line equivalent widths will hardly show detectable periodic variability. In fact, the modeled photometric amplitude, less than 6 mmag (Maintz et al. 2000), is in agreement with observations (Štefl et al. 1999). For the low  $v_{\text{rot}}$  set of parameters the photometric amplitude is of the same order of magnitude.

### 3.3. Absolute stellar parameters

Several determinations of fundamental stellar parameters of  $\omega$  CMa have been published.

From optical and infrared photometric measurements, taken shortly before an outburst in the late 70s and early 80s, Dachs et al. (1988) derived  $T_{\text{eff}} = 20\,000 \text{ K}$ ,  $\log g = 4.0$ , and  $R_{\star} = 5.2 R_{\odot}$  using  $E(B - V) = 0.06 \text{ mag}$ . The measured  $V$  magnitude was 3.81 and 3.92, respectively. For the same epoch, but using spectrophotometric data, Kaiser (1989) derived  $T_{\text{eff}} = 18\,600 \text{ K}$  and  $\log g = 3.4$  with  $E(B - V) = 0.04 \text{ mag}$ . Including also the envelope in the flux model, Dachs et al. (1989)

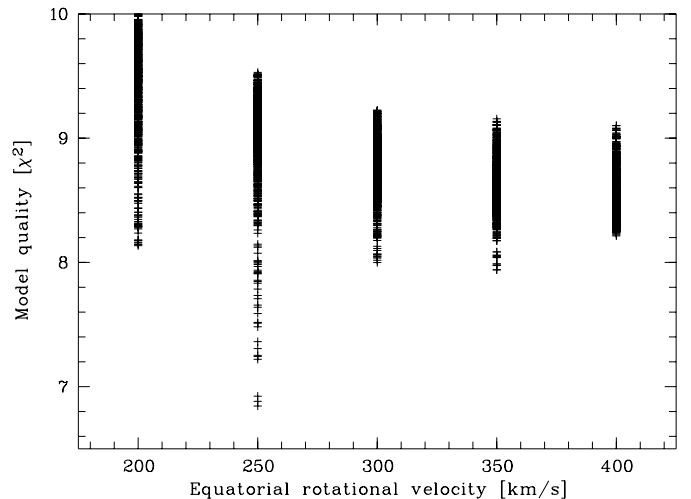


**Fig. 4.** The  $\chi^2$ -values of the coarse model grid (compared to the observations) plotted against the rotational velocity of the respective model. See Sects. 3.1.1 and 3.1.2 for discussion.

derived  $T_{\text{eff}} = 18\,000 \text{ K}$ ,  $\log g = 4.0$ , and  $R_{\star} = 5.2 R_{\odot}$  with a total (i.e. inter- and circumstellar)  $E(B - V) = 0.05 \text{ mag}$ .

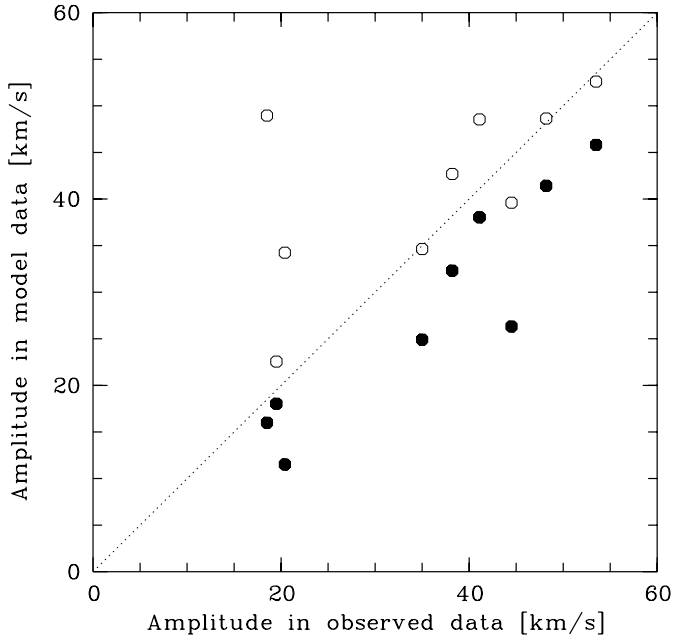


**Fig. 5.** Comparison of the line core velocity amplitudes, measured in the observational data (Paper II) vs. the lower  $v_{\text{rot}}$  (open circles, Table 1) and higher  $v_{\text{rot}}$  (filled circles, Table 2) models for a number of lines.

Harmanec (2000) got  $T_{\text{eff}} = 17\,100\text{ K}$  and  $R_{\star} = 9.91 R_{\odot}$ , based on the Hipparcos parallax of  $\pi = 3.53 \pm .58\text{ mas}$ ,  $V_0 = 4.0\text{ mag}$ , and spectral type vs. parameter calibrations, but did not publish which  $E(B - V)$  he used. If the spectrophotometric values mentioned above are recomputed using the Hipparcos distance and theoretical ATLAS 9 fluxes, radii close to the one obtained by Harmanec (2000) are derived.

Chauville et al. (2001), finally, derived  $T_{\text{eff}} = 21\,500\text{ K}$  and  $\log g = 3.81$ . This represents a surprisingly large range of parameters for such a bright and nearby star, but is not an unprecedented case: in  $\alpha$  Eri the very same is seen, which is most likely a consequence of almost critical rotation (Frémat et al. 2003).

Comparison with spectral line modeling in Figs. 2, 3, and 7 shows that  $T_{\text{eff}} = 18\,500\text{ K}$  and a  $\log g$  of about 3.5 (which is between the values in Tables 1 and 2) seem acceptably close to the true average surface parameters. The spectral type of B3 IV agrees with these parameters as well. Such a spectral type, however, is incompatible with a radius of almost  $10 R_{\odot}$  but, depending on which calibration is used, rather should be in the order of 5 to  $7 R_{\odot}$ , which is also the range of (polar) radii derived by  $nrp$  modeling.

The radius determinations depend on the measured and theoretical fluxes, and the distance. Although there are claims of systematic errors in the Hipparcos database (Pinsonneault et al. 1998), such errors are probably not required to explain the discrepancy. Looking at the LTPV photometry shown in Paper I, confirmed by Hipparcos photometry (see Fig. 8 in Harmanec 1998), the “quiescent ground state” is at least  $V = 4.05\text{ mag}$ , if not fainter. This means the spectrophotometric fluxes obtained by Dachs et al. (1989) have to be corrected not only for the

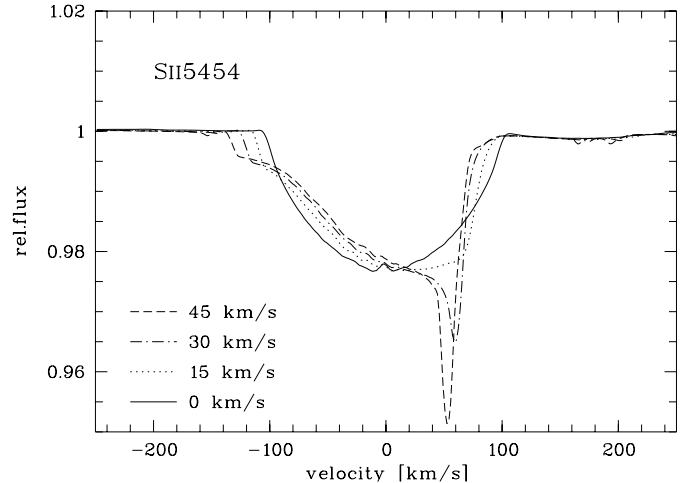


**Fig. 6.** Formation of a spike with increasing  $nrp$  amplitude ( $l = m = +2$ , at phase 0.0) in the example of S II 5454. The solid line represents the non-pulsating, but rotating profile. The small central bump is an effect of the latitudinal temperature variation due to gravity darkening. The blueshifted ramp exceeds the stellar  $v \sin i$  by about the velocity amplitude of the respective model, while the spike’s position is roughly at  $v \sin i$  minus this amplitude. Except the pulsation amplitude, the model parameters are those listed in Table 1.

extinction  $A_V$  of about 0.015 mag, but also for the envelope excess flux of about 0.13 mag.

The recomputation of the derived radius then becomes  $8.6^{+2.5}_{-1.5} R_{\odot}$ , taking into account both parallax errors and  $T_{\text{eff}}\text{-}\log g$  uncertainties. The parameters for the more rapidly rotating model (Table 2) lie well within this range. Also the lower radius-to-mass ratio of this parameter set is compatible with a subgiant star rather than the closer to ZAMS values in Table 1. All this, including the lower total pulsation amplitude of  $35\text{ km s}^{-1}$ , makes the higher  $v_{\text{rot}}$  parameters of Table 2 the favored ones in the end.

The intrinsic errors of the parameters derived by modeling the pulsational variability are related to the width of the minimum in the  $\chi^2$  distribution. Given the FWHM of the local minimum of the favored parameter set (Table 2), they are estimated to be roughly 1.5 times the stepwidth of the input grid, giving  $\sigma_{R_{\star}} = 0.75 R_{\odot}$ ,  $\sigma_{T_{\text{eff,polar}}} = 3000\text{ K}$ ,  $\sigma_{M_{\star}} = 1.5 M_{\odot}$ ,  $\sigma_{v_{\text{rot}}} = 75\text{ km s}^{-1}$ ,  $\sigma_i = 5^\circ$ , and  $\sigma_A = 8\text{ km s}^{-1}$ .

It should be noted that these error estimates disregard potential systematic errors, which to investigate would be beyond the scope of a paper dedicated to an individual star.

Determinations of the line width parameter  $v \sin i$  (interpreted as the projected rotational velocity) in the literature range from  $85 \pm 10\text{ km s}^{-1}$  (Chauville et al. 2001) to  $109 \pm 8$  (Yudin 2001), just bracketing our values for the projected rotational velocity in Table 1 and 2. So, from an observational point of view they seem in excellent agreement. However, one should keep in mind that the broadening function of the line profile is not the analytical one usually adopted in statistical studies, but both depending on the pulsation properties (see Fig. 7) and how close the object is to critical rotation. The example of  $\alpha$  Eri (Domiciano de Souza et al. 2003; Frémat et al. 2003) demonstrates that the classical techniques might underestimate the

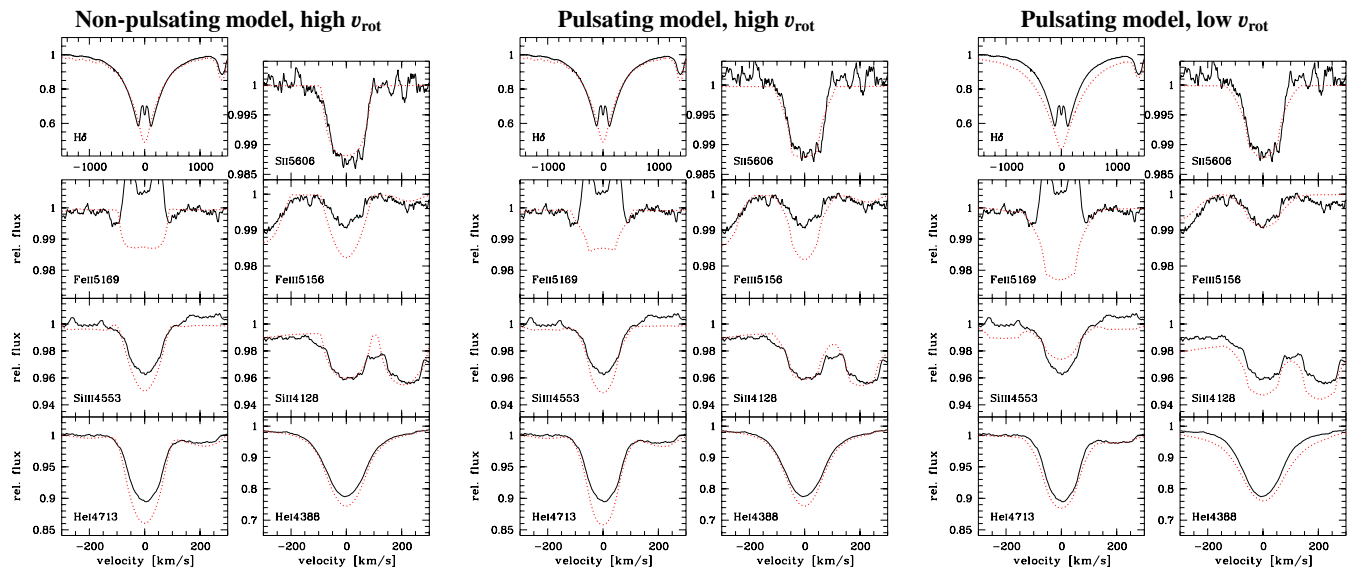


**Fig. 7.** The phase-averaged profiles as observed in  $\omega$  CMa (solid lines) compared to a non-pulsating model (left, based on parameters in Table 2, but amplitude zero), and the models with higher and slower rotation (for parameters see Tables 1 and 2). For a discussion see Sect. 3.3. All models show that line broadening is not generally the analytical one expected for rotational broadening, but a function of the pulsation amplitude and the rotational velocity (or better  $w = v_{\text{rot}}/v_{\text{crit}}$ , see Frémat et al. 2003).

rotational velocity if gravity darkening is not included. At the other hand, Fig. 7 shows that the same techniques may overestimate the rotation not taking into account pulsation. This is most obvious for weak lines (see Fe II 5169 in Fig. 7), but the effect is nevertheless also present in stronger lines.

#### 4. Formation of ramps and spikes

Spikes and ramps, as already found in  $\mu$  Cen (Rivinius et al. 2001b), result from a pole-on geometry in combination with high horizontal pulsation velocities in an  $|m| = 2$  mode in conjunction with a high amplitude of several tens of percent of the projected linewidth  $v \sin i$ . Since the movements on the stellar surface in  $\vartheta$  direction are not projected with  $\sin i$  (at variance to movements in  $\varphi$ , like rotation), the contrast of the  $lpv$  due to the pulsation will be enhanced for intermediate to low inclination angles, as long as the rotational broadening is still sufficient for Doppler mapping of the stellar surface. The velocity excess of the  $lpv$  beyond  $v \sin i$  is the total horizontal amplitude, that co-adds to the projected rotational velocity.

To illustrate the formation of these features, a set of models of S II 5454 was computed for the same pulsational phase (namely 0.0), but for different velocity amplitudes (Fig. 6). A spike becomes apparent with increasing amplitude at the red part of the line profile getting sharper and sharper. Corresponding to this spike, a ramp develops on the blue side of the profile. This combination can be explained by looking at the projected surface velocities. The projected surface velocity of a non-pulsating model ( $A = 0$ ) is a sine-wave shaped curve across the visible stellar disk, ranging from  $-v \sin i$  to  $+v \sin i$ . At the phase when the spike is formed, the pulsation velocity field of an  $|m| = 2$  mode, however, is rather of a hyperbolic shape. For instance, for the formation of a spike on the red side, like in Fig. 6 the projected pulsational velocity field will

be zero in the center and  $-A$  at both stellar limbs. Co-adding both fields gives a total velocity of  $-v \sin i + (-A)$  at the approaching limb of the star, causing the ramp at velocities exceeding  $v \sin i$  (namely by  $|A|$ ), while on the receding side the co-addition gives  $+v \sin i + (-A)$ . If  $A$  is sufficiently large, at least in the same order of magnitude as  $v \sin i$ , this causes the steep shoulder of the profile at the red edge and the spike, because no part of the visible hemisphere will be seen at full  $v \sin i$  and in turn a larger fraction of the stellar disk will be projected into the spike's velocity range than without pulsation (Fig. 8).

The presence of spikes and ramps can thus be explained naturally as due to high amplitude  $g$ -mode pulsation of  $|m| = 2$  in a pole-on seen star within the scope of non-radial pulsation. In modes with higher  $|m|$  it depends whether  $|m|$  is even or odd. In the first case, basically similar features will appear, though weaker. For the latter, spikes at both sides will simultaneous present, so will be ramps half a cycle later. In both cases, additional subfeatures within the line profile will be present. The requirement of high horizontal amplitude limits the possible modes to retrograde ones in Be stars: For prograde modes either the co-rotating period is quite short, so that the ratio of horizontal-to-vertical amplitude becomes small (i.e. the mode is getting  $p$ -mode characteristics) and the pulsational motions are dominated by the vertical ones. The necessary high horizontal amplitudes would require full amplitudes likely to disrupt the star if these modes were prograde in Be stars.

#### 5. Periodic line profile variability during outbursts

In Paper II it was shown that the  $lpv$  of some lines changes during outbursts. For these lines the prograde traveling bump weakens or even disappears, and the retrograde traveling feature strengthens (Fig. 9, observed data, see also Paper II). The lines with typically strong circumstellar emission

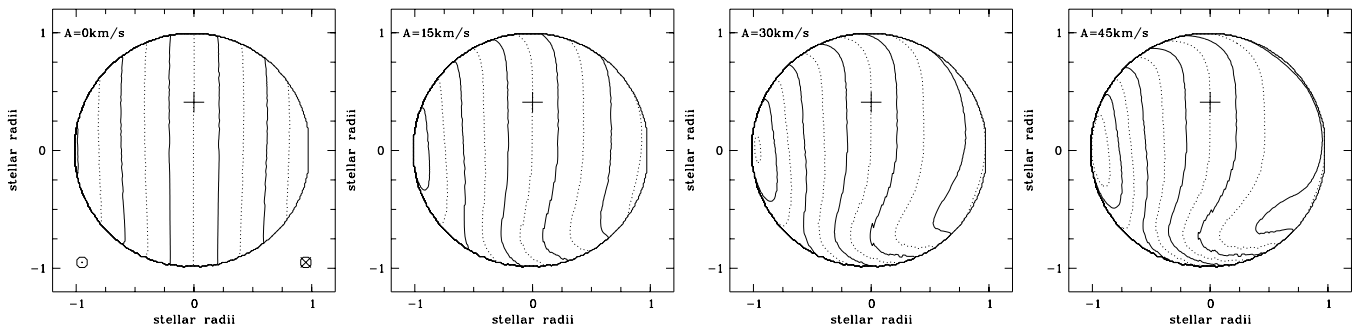


**Fig. 8.** Contours of the projected velocity field for a pole-on non-radial pulsator (see Table 1), corresponding to the profiles shown in Fig. 6. Contours are plotted every  $20 \text{ km s}^{-1}$ , from  $-100$  to  $+100 \text{ km s}^{-1}$ . The stellar pole is marked by a cross and also marks the zero projected velocity contour. Note that for plotting purpose the geometrical deformations were neglected. The leftmost panel shows the pure rotational velocity field, indicating also the sense of rotation by symbols in the lower corners. In case of pulsation, the projected velocities are enhanced at the approaching (i.e. left) limb wrt. to pure rotation, causing the ramp. In the highest amplitude model, the  $-120 \text{ km s}^{-1}$  contour becomes visible there, while at the receding right limb high velocities are suppressed, so that no velocities above  $+80 \text{ km s}^{-1}$  are seen on the surface. Therefore, on the receding hemisphere a large visible surface area has very little dispersion in projected velocity, causing the spike in the resulting line profile (see Fig. 6).

contribution, like the Balmer lines, O I 8446, and Fe II 5169 are affected most, while lines like Mg II 4481 show a weaker effect and purely photospheric lines like Si III 4553 remain unaffected. Since this behavior has been observed in both the 1996 and 2001 outbursts, it is likely to be a general property of outbursts of  $\omega$  CMa and, presumably, of the outbursts in other (low  $v \sin i$ ?) Be stars as well.

One possibility to explain this is certainly interaction of the variable photosphere with the disk, which at times of outbursts reaches down to the star itself (Rivinius et al. 2001a). This could either be some “lighthouse effect” as proposed by Penrod (1986) or the extension of the pulsational velocity field into the disk due to mass-loss (wave leakage).

But there might be another mechanism that could explain this behavior with fewest possible additional assumptions. The disk, being in contact with the photosphere during an outburst, is optically thick at least in the Balmer lines and, though less, probably also in the other mentioned lines (Millar et al. 2000). Assuming this has no effect on the pulsation itself, supported by the largely unchanged behavior of lines like Si III 4553 (except a slow phase drift, see Paper II), the disk will veil the equatorial region as seen by the observer, but only for optically thick lines. This, however, can easily be tested with an *nrp* model: Only points on the stellar disk above some stellar colatitude  $\vartheta$  are taken into account by KYLIE for computing the observable spectrum (Fig. 9).

In fact, the basic behavior of H $\delta$  and similar lines is reproduced by such a “ $\vartheta$ -limited” model. To create this effect, the star needs to be veiled up to quite high colatitudes of about  $30^\circ$  to  $40^\circ$  above the equator. Though this seemingly contradicts results that Be star disks only have less than  $\approx 20^\circ$  degree opening angle at the inner edge (Hanuschik 1996; Quirrenbach et al. 1997), the disk is certainly not in an equilibrium configuration during an outburst.

This would mean that the disk is optically completely thick in the Balmer and similar lines, and relatively optically thin in the continuum. There might still be some scattering of light even for photons originating from lines like Si III 4553, but this

does not destroy the line profile completely. On the other hand, at least some scattering in the continuum is also required to explain the light changes during outbursts. Polarization measurements indeed typically derive electron optical depths  $\tau_e$  of the order of unity (e.g. McDavid 2001).

However, such a modified model does not completely explain the observed variability. The  $\vartheta$ -limited variability should become weaker compared to the full-disk one, (see Fig. 9, overplots of the residual variability) while it is in fact observed to be even stronger in H $\delta$ . Similarly, the velocity range of the *lpv* should become narrower, but this is not observed, again in H $\delta$  it becomes even wider. The mean profile of the H $\delta$  during and outside outburst differs by higher wings, possibly due to enhanced Thompson scattering (see Paper I, their Fig. 3). While the model does not look too bad for Mg II 4481 and similar lines, at least in H $\delta$  (and the other Balmer lines) additional variability must be present, that still may require to invoke star-disk interaction mechanisms as discussed above.

## 6. Conclusion

The photospheric *lpv* of  $\omega$  CMa was modeled as non-radial pulsation for spectral lines of nine different ions, using the simulation codes BRUCE and KYLIE by Townsend (1997b). The adopted pulsation mode is  $\ell = 2, m = +2$  with a negative observer’s period. This means that the pulsation, being retrograde in the corotating frame, is seen prograde in the observer’s frame due to the rapid rotation.

The residual variability is reproduced in high detail in all modeled lines, regardless if those lines have emission contribution or not. This concurs with the finding by Štefl et al. (2002) that HR 4074, a star of similar spectral type and  $v \sin i$  as  $\omega$  CMa, shows almost identical *lpv*, although the only reported emission episode of this Be stars dates back more than a century. Since it is hardly believable that HR 4074 could have maintained any circumstellar material without showing line emission for such a time, its *lpv* must be of photospheric origin.

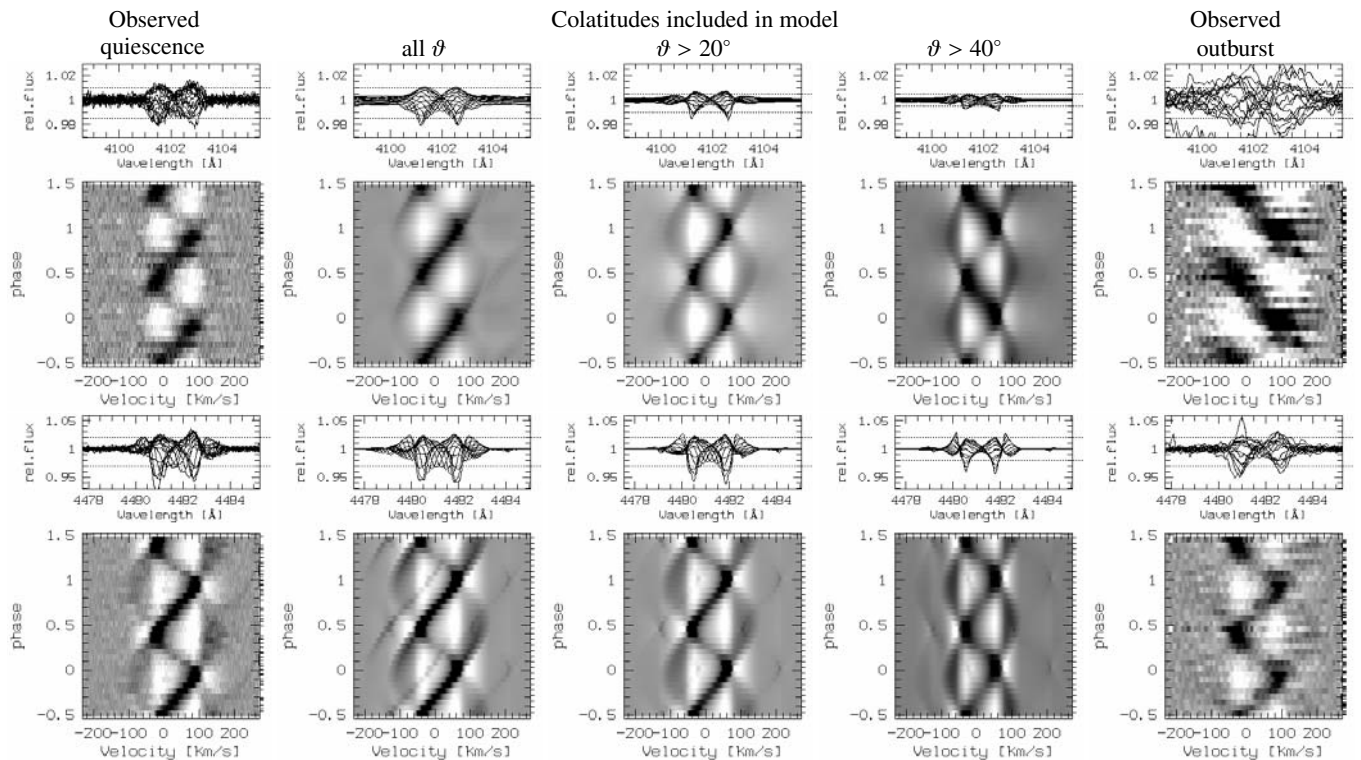


**Fig. 9.** Line profile-variability during quiescence and outburst for H $\delta$  (top row) and Mg II 4481 (bottom row). To the very left and right observations during quiescence and outburst are shown, respectively. In the middle columns the model (lower  $v_{\text{rot}}$ , Table 1) is shown if the entire visible hemisphere is integrated (all  $\vartheta$ ), and if only stellar latitudes above  $20^\circ$  and  $40^\circ$ , respectively, are taken into account. See Sect. 5 for a physical interpretation.

Although the absolute line profiles are not reproduced equally well as the residual  $lpv$ , this can be attributed to mismatches of the global stellar parameters, for which no unique solution could be found. In any case, this is not a problem of the  $nrp$  hypothesis itself. For general astrophysical considerations (Sect. 3.3), however, the stellar parameters presented in Table 2 are preferred as final ones, although the  $lpv$  is reproduced with not quite as high accuracy as with the parameters shown in Table 1.

The modified  $lpv$  of several lines with circumstellar emission contribution during outbursts can be reproduced by the model if a veiling effect of the circumstellar disk on the photosphere is assumed, so that only the photospheric variability above stellar co-latitudes of about  $30^\circ$  to  $40^\circ$  is visible to the observer.

An alternative hypothesis attributes the  $lpv$  of  $\omega$  CMa (Balona et al. 1999) to “patches” on the stellar surface. The only, quite parametric, modeling for this hypothesis was attempted for  $\omega$  CMa by Balona et al. (1999). Neglecting the possibility of  $\text{sign}(\sigma_{\text{obs.}}) = -1$ , these authors did not succeed in modeling the  $lpv$  with the BRUCE/KYLIE codes (also used in this paper) and therefore excluded  $nrp$ . But assuming a non-uniform distribution of photospheric microturbulence (called patches), they could reproduce the relatively weak spikes in He I 6678, but did not take into account the ramps for the modeling, since their velocity is higher than  $v \sin i$ . As shown by Maintz et al. (2000) and in this work, however, both spikes and ramps can naturally be explained as consequences

of non-radial pulsation under the given circumstances. Later, (Balona 2000) favoured a corotating cloud instead, also for Be stars in general, but the above sketched argument favoring a photospheric origin of the  $lpv$ , like in HR 4074, contradicts the cloud hypotheses as well.

Also the fact that  $\omega$  CMa shows a very small photometric amplitude with the  $lpv$  period, but the strongest  $lpv$  known in all Be stars does not require further assumptions but is naturally explained by  $nrp$ . Other pole-on Be stars are similar cases showing strong  $lpv$  without detectable photometric periodicity, including HR 4074. These modeling results were achieved on the basis of generally accepted, general-purpose  $nrp$ - and atmosphere models, not assuming more free parameters than for modeling any other pulsating star.

It can be concluded that  $\omega$  CMa is a non-radially pulsating Be star, and that non-radial pulsation is sufficient to explain the observed periodic photospheric  $lpv$  entirely. The detailed  $nrp$ -modeling of  $\mu$  Cen (Rivinius et al. 2001b) and  $\omega$  CMa in this work provide firm ground for the conclusion drawn by Rivinius et al. (2002a), namely that (early-type) Be stars form a homogeneous group of non-radial pulsators.

*Acknowledgements.* We thank the referee, A.-M. Hubert, for helpful and constructive suggestions to improve the manuscript. Financial support was granted by the DFG (Wo 296/20, Ap 19/7, 436 TSE 113/18 and 41), and the Academy of Sciences and Grant Agency of the Academy of Sciences of the Czech Republic (436 TSE 113/18 and 41, AA3003001, K2043105).

This study made use of the Simbad and ADS databases.

## References

- Baade, D. 1982, *A&A*, 105, 65
- Balona, L. A. 2000, in ASP Conf. Ser. 214, *The Be Phenomenon in Early Type Stars*, IAU Colloq., 175, 1
- Balona, L. A., Aerts, C., & Štefl, S. 1999, *MNRAS*, 305, 519
- Chauville, J., Zorec, J., Ballereau, D., et al. 2001, *A&A*, 378, 861
- Dachs, J., Kiehling, R., & Engels, D. 1988, *A&A*, 194, 167
- Dachs, J., Poetzl, R., & Kaiser, D. 1989, *A&AS*, 78, 487
- Domiciano de Souza, A., Kervella, P., Jankov, S., et al. 2003, *A&A*, 408, L47
- Frémat, Y., Zorec, J., Hubert, A., et al. 2003, in IAU Symp. 215, *Stellar Rotation*, in press
- Gummersbach, C. A., Kaufer, A., Schäfer, D. R., Szeifert, T., & Wolf, B. 1998, *A&A*, 338, 881
- Hanuschik, R. W. 1996, *A&A*, 308, 170
- Harmanec, P. 1998, *A&A*, 334, 558
- Harmanec, P. 2000, in ASP Conf. Ser. 214, *The Be Phenomenon in Early Type Stars*, IAU Colloq., 175, 13
- Kaiser, D. 1989, *A&A*, 222, 187
- Kaufer, A., Stahl, O., Tubbesing, S., et al. 1999, *ESO Messenger*, No. 95, 8
- Ledoux, P. 1951, *ApJ*, 114, 373
- Maintz, M., Rivinius, Th., Tubbesing, S., et al. 2000, in ASP Conf. Ser. 214, *The Be Phenomenon in Early Type Stars*, IAU Colloq., 175, 244
- McDavid, D. 2001, *ApJ*, 553, 1027
- Millar, C. E., Sigut, T. A. A., & Marlborough, J. M. 2000, *MNRAS*, 312, 465
- Penrod, G. D. 1986, *PASP*, 98, 35
- Pinsonneault, M. H., Stauffer, J., Soderblom, D. R., King, J. R., & Hanson, R. B. 1998, *ApJ*, 504, 170
- Quirrenbach, A., Bjorkman, K. S., Bjorkman, J. E., et al. 1997, *ApJ*, 479, 477
- Rivinius, Th., Baade, D., Štefl, S., & Maintz, M. 2001a, *A&A*, 379, 257
- Rivinius, Th., Baade, D., Štefl, S., et al. 2001b, *A&A*, 369, 1058
- Rivinius, Th., Baade, D., Štefl, S., & Maintz, M. 2002a, in ASP Conf. Ser. 259, *Radial and Nonradial Pulsations as Probes of Stellar Physics*, IAU Colloq. 185, 240
- Rivinius, Th., Baade, D., Štefl, S., Maintz, M., & Townsend, R. H. D. 2002b, *ESO Messenger*, 108, 20
- Rivinius, Th., Baade, D., & Štefl, S. 2003, *A&A*, 411, 229
- Štefl, S., Aerts, C., & Balona, L. A. 1999, *MNRAS*, 305, 505
- Štefl, S., Baade, D., Rivinius, Th., Otero, S., & Setiawan, J. 2001, *IAU Information Bulletin on Variable Stars*, No. 5193
- Štefl, S., Rivinius, Th., & Baade, D. 2002, in ASP Conf. Ser. 259, *Radial and Nonradial Pulsations as Probes of Stellar Physics*, IAU Colloq., 185, 248
- Štefl, S., Baade, D., Rivinius, Th., et al. 2003a, *A&A*, 411, 167 (Paper II)
- Štefl, S., Baade, D., Rivinius, Th., et al. 2003b, *A&A*, 402, 253 (Paper I)
- Townsend, R. H. D. 1997a, Ph.D. Thesis, University College London
- Townsend, R. H. D. 1997b, *MNRAS*, 284, 839
- Yudin, R. V. 2001, *A&A*, 368, 912